Electronic Supplementary Material (ESI) for Nanoscale.
This journal is © The Royal Society of Chemistry 2020

Supporting Information

Solution-phase vertically growth of aligned $NiCo_2O_4$ nanosheets arrays on Au nanosheets with weakened oxygen-hydrogen bond for photocatalytic oxygen evolution

Suisui He[a†], Jian Chai[b†], Siyu Lu[c], Xijiao Mu[b], Ruitong Liu[a], Qiang Wang[a], Fengjuan Chen[a], Yuee Li*[,b], Jingang Wang[d], Baodui Wang*[,a]

[a]*State Key Laboratory of Applied Organic Chemistry, Key Laboratory of Nonferrous Metal Chemistry and Resources Utilization of Gansu Province, College of Chemistry and Chemical Engineering, Lanzhou University, Lanzhou, 730000, P. R. China.*

[b]*School of Information Science and Engineering, Lanzhou University, Lanzhou 730000, China.*

[c]*College of Chemistry and Molecular Engineering, Zhengzhou University, Zhengzhou, 450001, China*

[d]*Liaoning Shihua University, Fushun 113001, China.*

[†]Suisui He and Jian Chai contributed equally to this work.

[*]Corresponding author.

E-mail address: liyuee@lzu.edu.cn; wangbd@lzu.edu.cn.

Experimental Detail

Characterizations. Field-emission scanning electron microscope (FE-SEM, FEI, Sirion 200), transmission electron microscope (TEM, Tecna i-G2-F30 (FEI)), X-ray powder diffraction (XRD, AXS D8-Advanced diffractometer), X-ray photoelectron spectroscopy (XPS, a PHI-5702 multifunctional spectrometer), were used to characterize the morphology and composition of the material. UV-vis absorbance measurements were recorded on Shimadzu UV-1750. Photocatalysis was performed using Xenon lamp (HSXF/UV 300), equipped with 400-800 nm filter. Photoluminescence (PL) spectra were acquired on an Edinburgh Instruments FLS920 fluorescence spectrometer. For the measurement of PL lifetime, the used excitation wavelength (λex) was 270 nm and the maximum emission wavelength (λem) was 370 nm. The average lifetime (Ave. τ) is calculated according to $\tau = \tau 1 \cdot I1 + \tau 2 \cdot I2 + \tau 3 \cdot I3$ (τi is the lifetime; Ii is the relative intensity).[1,2] Time-resolved transient absorption spectra (TAS) was performed in femtosecond transient absorption spectroscopy. The laser source was a Coherent Legend Elite regenerative amplifier (<110 fs, 1 KHz, 800 nm), which was seeded by a Coherent Chameleon oscillator (75 fs, 80 MHz). The 400 nm pump pulses were got by doubling partial of the fundamental 800 nm pulses with a BBO crystal. The white probe pulses in 425-800 nm range were generated on a sapphire crystal excited through partial of the 800-nm laser beam from the amplifier.

The apparent quantum efficiency (AQE) measurement. A 300 W Xe lamp was used as the light source for photocatalytic reaction. The measurement of AQE was performed using same amount reactions. We fixed the wavelength at 450 ± 10, 500 ± 10, 550 ± 10, 600 ± 10, 650 ±10, 700 ± 10 and 800 ± 10 for irradiation. The laser power in the photocatalytic reaction was collected using a power meter (Newport; 843-R). The corresponding wavelength captured for AQE calculation are located at 450 ± 10 nm. Thus, the AQE was calculated as the following equation, AQE = 4n/np × 100 %, in which n and np were denoted as the number of photos that generating product needed and the number of incident photons, respectively. The AQE for the catalysts under light irradiation at the wavelength of others were also calculated with the same method.

The apparent quantum efficiency (AQE) calculation. Under visible light irradiation (450 ± 10 nm) for $NiCo_2O_4$-Au-$NiCo_2O_4$ sandwich-type heterojunctions within 30 min. The average intensity of irradiation was found to be 0.114 W and 0.0672 W before and after the catalyst added to reaction flask by a power meter (Newport; 843-R). Total absorb light energy $\Delta E = (0.114-0.0672) \times 30 \times 60 = 84.24$ J, n = 0.0173 mmol, energy per photon $E_0 = hc/\lambda = 6.63 \times 10^{-34} \times 3 \times 10^8/(450 \times 10^{-9}) = 4.42 \times 10^{-19}$ J, molor of photons $np=\Delta E/(E_0 \times NA) = 84.24/(4.42 \times 10^{-19} \times 6.02 \times 10^{23}) = 0.316$ mmol, AQE (initial) = 4n/np = 4 × 0.0173/0.316 × 100% = 21.9%. With the same method, we can calculate the initial AQE for other light irradiation, the AQE (initial) were 14.2%, 13.9%, 10.5%, 6.8%, 6.33% and 5.0%, respectively.

Photoelectrochemical measurement. Photoelectrochemical properties were performed on an electrochemical station (CHI 760E) in a standard three-electrode, single-compartment quartz cell. The Au nanosheets electrode, $NiCo_2O_4$ nanosheets electrode and the $NiCo_2O_4$-Au-$NiCo_2O_4$ sandwich-type heterojunctions electrode with an active area of 1 cm^2 served as the working electrodes. The counterelectrode and reference electrode consisted of a platinum sheet (99.99 %, 0.1 mm, 1 cm × 2 cm) and Ag/AgCl, respectively. Photoelectrochemical measurements were collected under visible light illumination (λ>420 nm filter, 300 W Xe lamp) in a 0.1 M Na_2SO_4 (pH=13) solution. And the Xe lamp was positioned 10 cm away from the photoelectrochemical cell. The transient photocurrent was measured using a 50 s onoff cycle at a bias voltage of 0.8 V.

DFT Calculations. The spin-polarized DFT calculations were performed using projector augmented wave (PAW) potentials and the Perdew-Burke-Ernzarhof (PBE) functional implemented in the Vienna ab initio simulation package (VASP)[3-5]. The $NiCo_2O_4$ (311) surface with two atomic layers and Au (111) surface with four atomic layers were modeled as a p (2×4) periodic slab, respectively, in the unit cell of the Au-$NiCo_2O_4$ heterojunctions. In order to simulate bulk proprieties, Au atoms in the bottom layer were fixed, and all other atoms were fully relaxed. The neighboring layers were separated in the direction perpendicular to the surface by a vacuum distance of 18 Å, which removes the effects of periodic structures, we choose the energy convergence as 1×10^{-6} eV $atom^{-1}$. Monkhorst-Pack grids of special points with 1×3×1 meshes were used for Brillouin-zone integrations. The kinetic-energy cutoff of the plane wave was set to 750 eV.

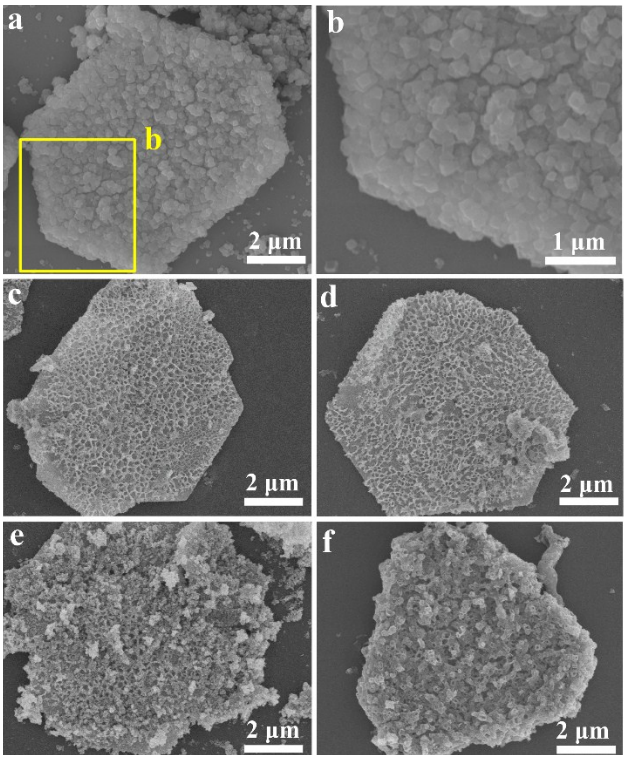

Figure S1. (a,b) SEM images of Ni-Co acetate hydroxide-Au-Ni-Co acetate hydroxide heterostructures at different magnifications. SEM images of $NiCo_2O_4$-Au-$NiCo_2O_4$ sandwich-type heterojunctions at different concentrations of $NaBH_4$: (c) 0.05 M, (d) 0.20 M, and (e) 0.80 M. (f) SEM image of $NiCo_2O_4$-Au-$NiCo_2O_4$ sandwich-type heterojunctions at 0.05 M $NaBH_4$.

As shown in **Figure S1a** and **S1b**, after ultrasonic treatment, the Au nanosheet surface was covered by Ni-Co acetate hydroxide nanoparticles. Then the formed Ni-Co acetate hydroxide-Au-Ni-Co acetate hydroxide heterostructures are chemically converted into Ni-Co hydroxide ultrathin nanosheet-Au-Ni-Co hydroxide ultrathin nanosheet heterostructures by treatment with $NaBH_4$. Finally, the above heterojunctions were calcinated at 400 ^{o}C in air to obtain $NiCo_2O_4$-Au-$NiCo_2O_4$ sandwich-type heterojunctions.

To study the role of $NaBH_4$ in the formation of $NiCo_2O_4$ nanosheets, different concentrations of $NaBH_4$ were added to observe the morphological changes. As shown in **Figure S1c-e**, with increasing the concentration of $NaBH_4$, the thickness of the $NiCo_2O_4$ nanosheets gradually becomes thinner and collapses. And other basic additives, such as NaOH were used to study the role of $NaBH_4$. As shown in **Figure S1f,** the thickness of the $NiCo_2O_4$ nanosheets increased and the channels formed by interconnected nanosheets became smaller. It is well known that H_2 and NaOH will be produced simultaneously in $NaBH_4$ aqueous solution. These results explicitly demonstrate the important role of H_2 in the formation of ultrathin Ni-Co acetate hydroxide nanosheets.

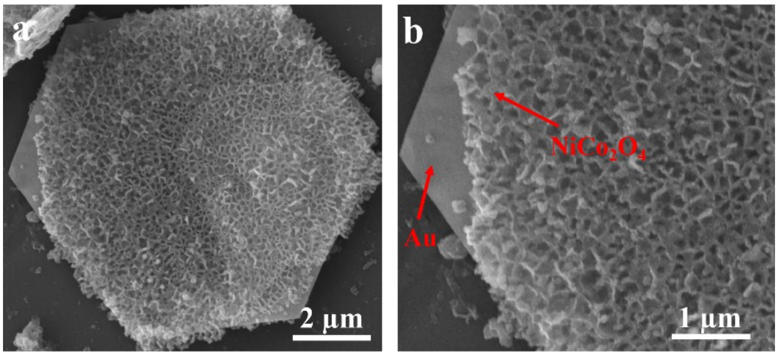

Figure S2. SEM images at different magnifications (a and b) of partially broken $NiCo_2O_4$-Au-$NiCo_2O_4$ sandwich-type heterojunctions in the presence of small amounts of hydrochloric acid.

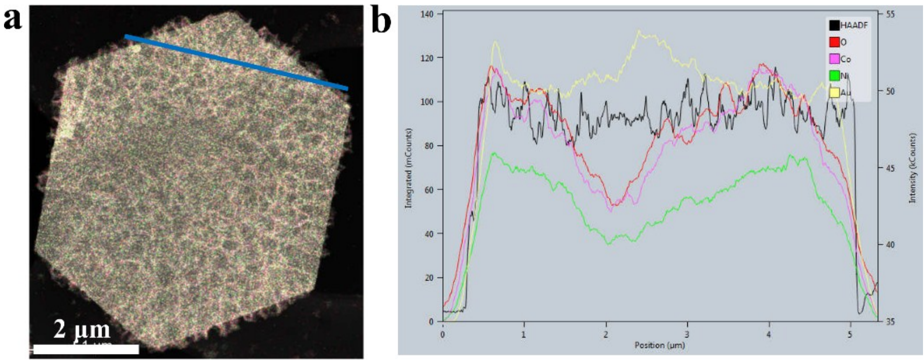

Figure S3. (a) STEM-HAADF image of $NiCo_2O_4$-Au-$NiCo_2O_4$ sandwich-type heterojunctions. (b) Line profiles of elemental compositions measured by EDX along the line shown on image.

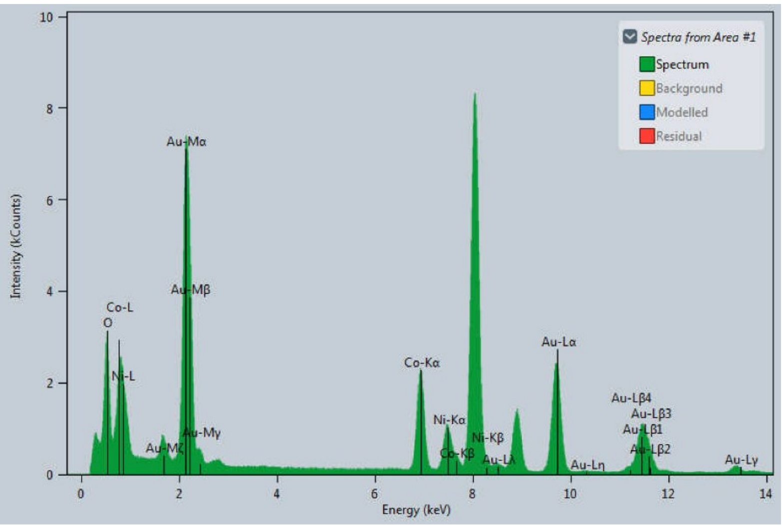

Figure S4. EDX of $NiCo_2O_4$-Au-$NiCo_2O_4$ sandwich-type heterojunctions.

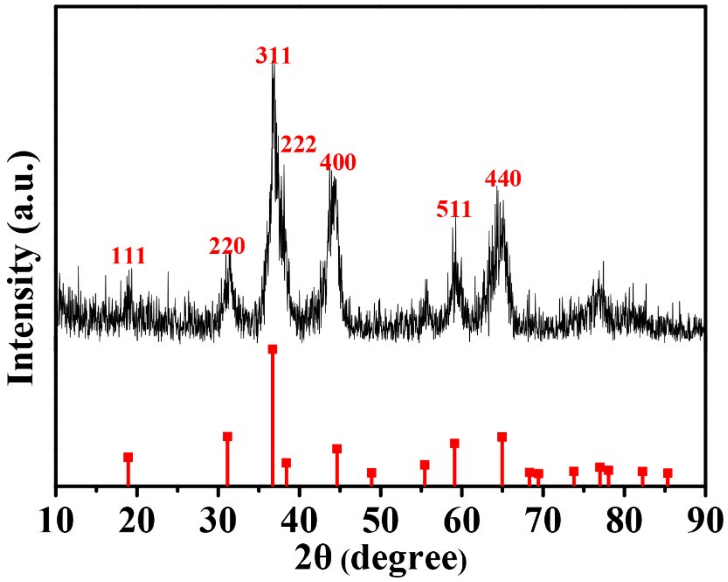

Figure S5. (a) XRD patterns of $NiCo_2O_4$ nanosheets without Au nanosheets. (Red color indicates the diffraction planes of $NiCo_2O_4$.)

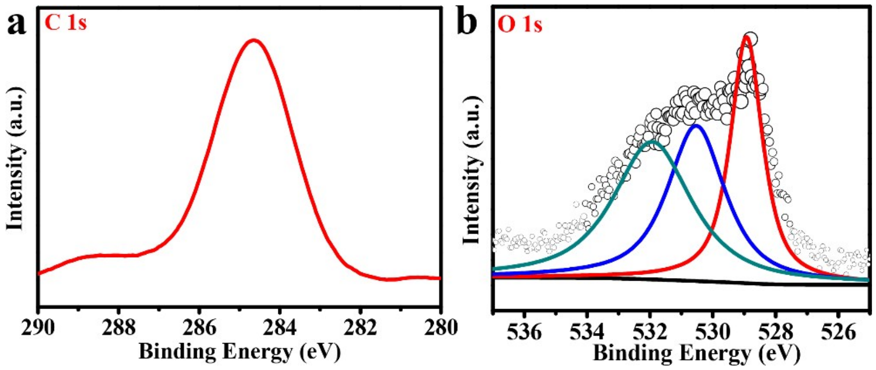

Figure S6. XPS spectra of $NiCo_2O_4$-Au-$NiCo_2O_4$ sandwich-type heterojunctions: (a) C 1s, (b) O 1s.

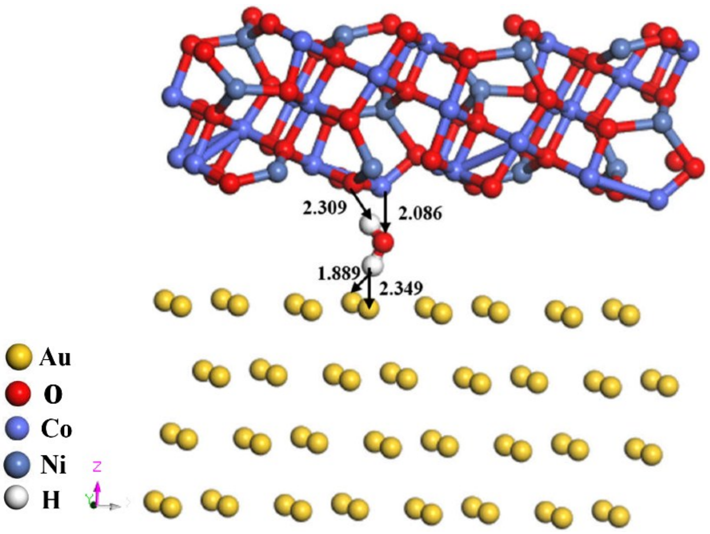

Figure S7. Optimized $NiCO_2O_4$@Au@H_2O distance between different atoms.

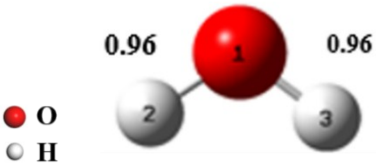

Figure S8. Optimized H_2O distance between different atoms and Mayer band order. The present calculations were executed with a version of Gaussian 09[6]. Geometry optimizations was performed with B3LYP[7] and 6-31G** basis set.

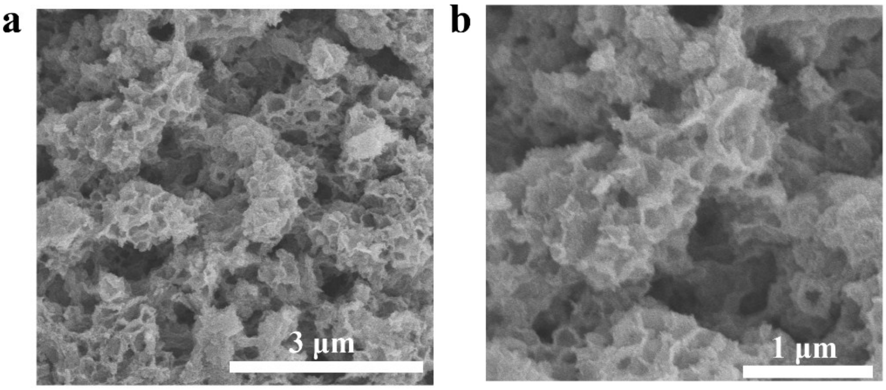

Figure S9. SEM images at different magnifications of $NiCo_2O_4$ nanosheets without Au nanosheets.

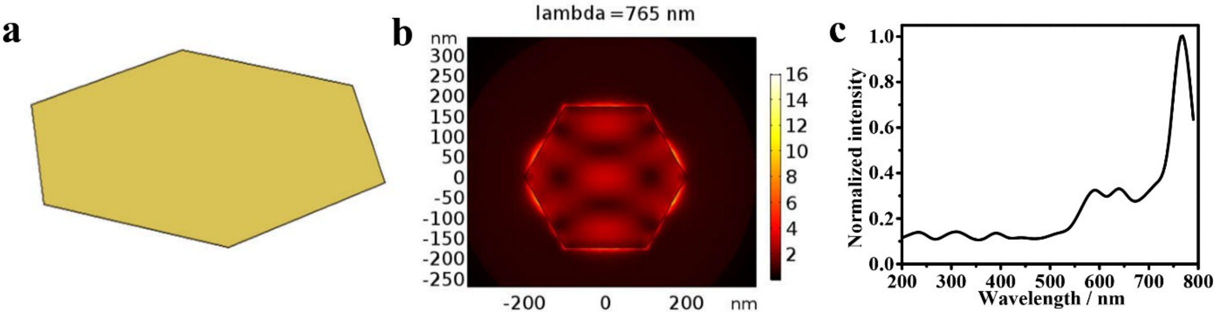

Figure S10. (a) Au nanosheet model that we built for calculation; (b) Electric field distribution |E| upon 765 nm excitation with plane wave incidence (E0=1 V/m); (c) Normalized average electronic field intensity along with the excitation wavelength.

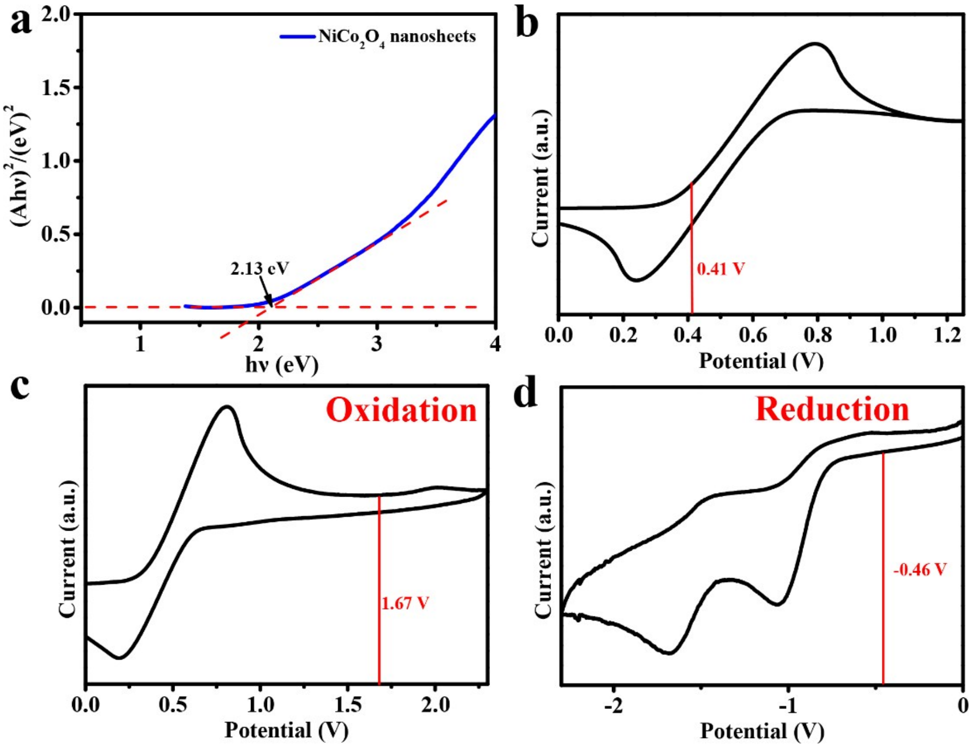

Figure S11. (a) Optical band gap energy of $NiCo_2O_4$ nanosheets obtained by extrapolation to $(\alpha h\nu)^2 = 0$. (b) The cyclic voltammograms (CV) of the oxidation potential of ferrocene as the internal standard to calibrate the measurements, and (c) oxide and (d) reduction CV of $NiCo_2O_4$ nanosheets.

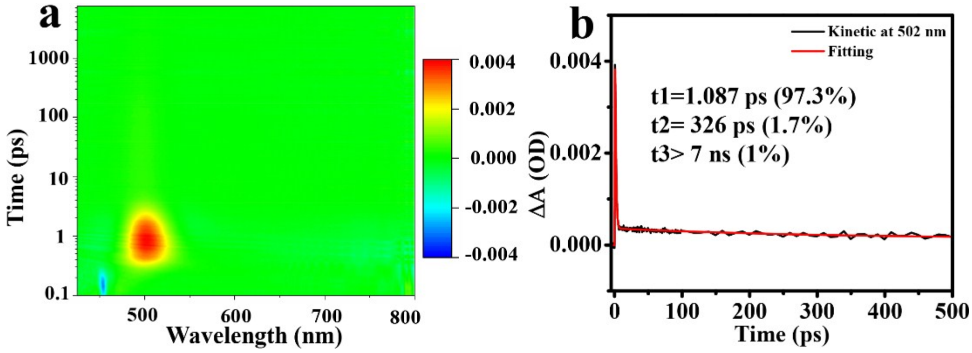

Figure S12. (a) 3D plot time-resolved TAS of Au nanosheets upon 400 nm lase excitation. (b) Kinetic profiles of Au nanosheets at 502 nm in the ps region upon 400 nm laser excitation.

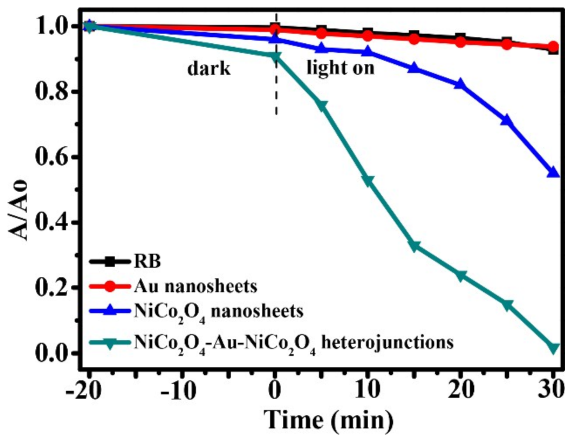

Figure S13. Photocatalytic degradation efficiencies of different catalysts toward RB measured by UV-vis adsorption spectrum.

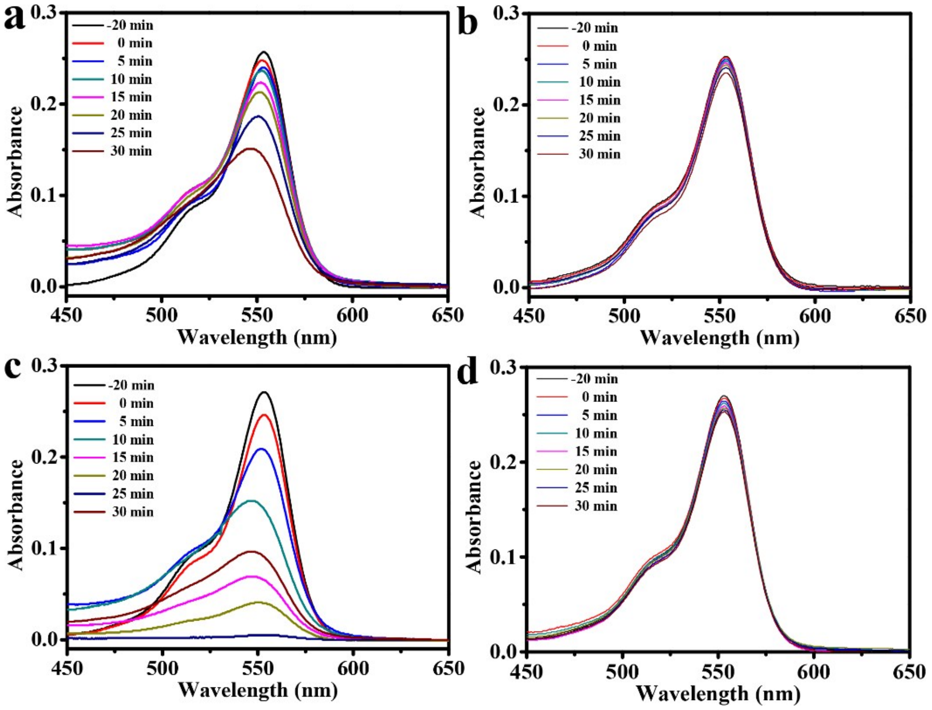

Figure S14. Absorption spectroscopy of (a) $NiCo_2O_4$ nanosheets, (b) Au nanosheets, (c) $NiCo_2O_4$-Au-$NiCo_2O_4$ sandwich-type heterojunctions and (d) single RB on the degradation of RB in the dark for 20 min and under visible light irradiation for 30 min. (The mixture stirred in the dark for 20 min was to reach adsorption/desorption equilibrium.)

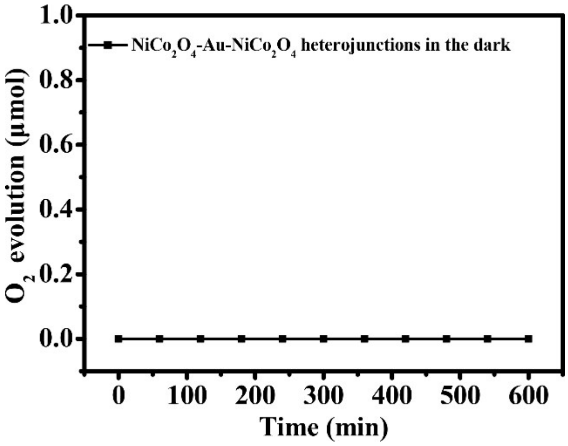

Figure S15. Oxygen evolution performance of $NiCo_2O_4$-Au-$NiCo_2O_4$ sandwich-type heterojunctions at 30 ℃ in the dark.

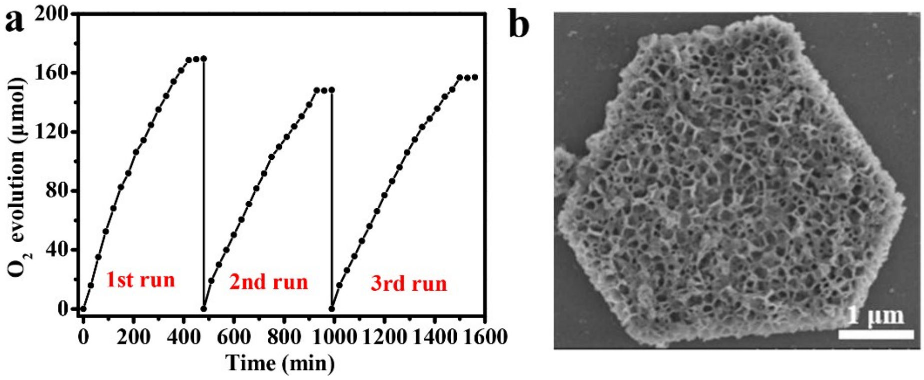

Figure S16. (a) Photocatalytic stability test of $NiCo_2O_4$-Au-$NiCo_2O_4$ sandwich-type heterojunctions. (b) SEM of $NiCo_2O_4$-Au-$NiCo_2O_4$ trilayered heterojunctions after the three cycles tests.

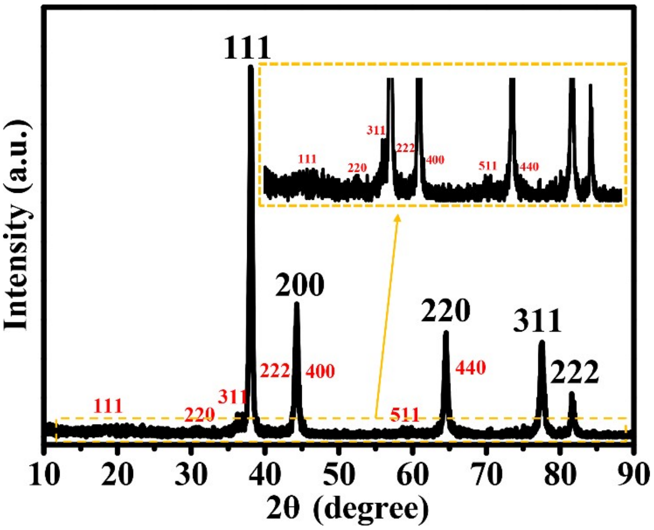

Figure S17. XRD patterns of $NiCo_2O_4$-Au-$NiCo_2O_4$ sandwich-type heterojunctions after the three cycles tests. Compared to the $NiCo_2O_4$-Au-$NiCo_2O_4$ trilayered heterojunctions before tests, the catalyst still keeps original appearance although a small amount of collapse, which means the catalyst has good stability.

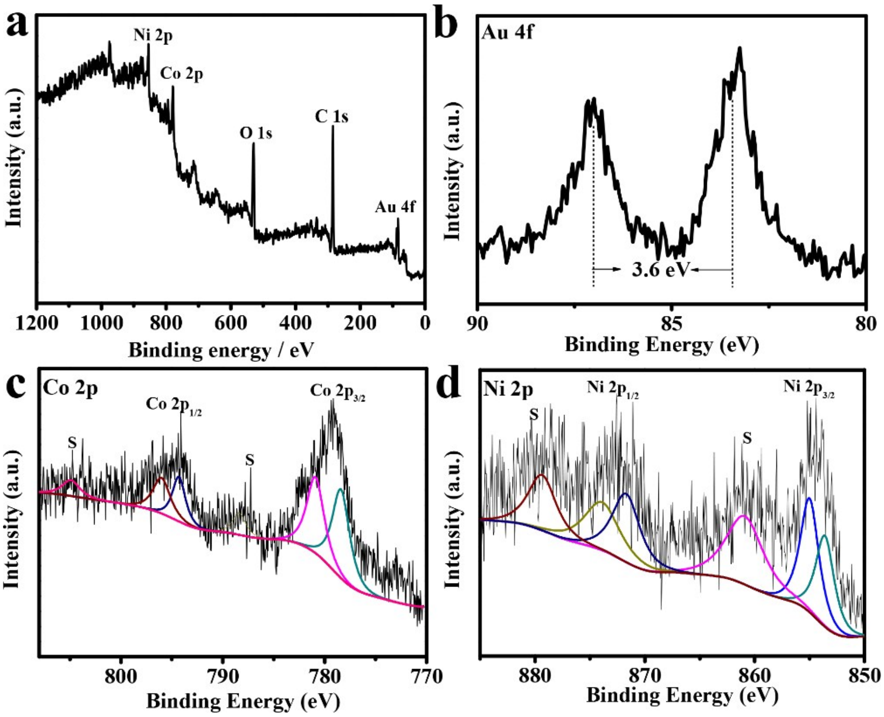

Figure S18. XPS spectra of $NiCo_2O_4$-Au-$NiCo_2O_4$ sandwich-type heterojunctions after three cycles: (a) full spectrum, (b) Au 4f, (c) Co 2p, (d) Ni 2p.

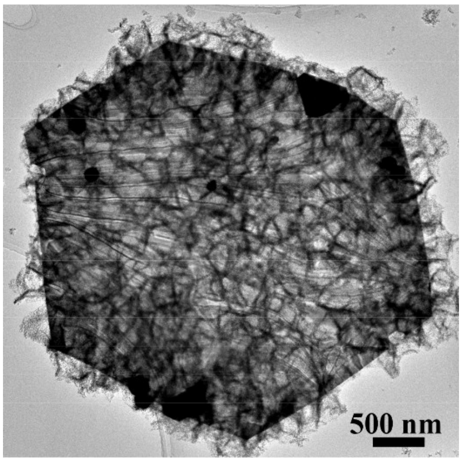

Figure S19. TEM image of $NiCo_2O_4$-Au-$NiCo_2O_4$ sandwich-type heterojunctions after three cycles.

Table S1. Analysis of the charge of Au nanosheets and the surrounding Ni, Co, H, O atoms with Au atoms.

Type of atoms	Actual charge number (n_A)	Theoretical charge number (n_T)	Transferred charge number (n)
Co 3	7.79	9	1.21
Ni 3	8.99	10	1.01
Co 4	7.80	9	1.20
Au 13	11.04	11	0.04
Au 13	11.04	11	0.04
Co 23	8.04	9	0.96
O 49	7.18	6	1.18
H 1	0.38	1	0.62
H 2	0.49	1	0.51

Table S2. Analysis of the charge of Au nanosheets and the surrounding Ni, Co atoms with Au atoms.

Type of atoms	Actual charge number (n_A)	Theoretical charge number (n_T)	Transferred charge number (n)
Co3	8.03	9	0.97
Ni3	9.17	10	0.83
Co4	8.03	9	0.97
Au13	11.02	11	0.02
Au13	11.01	11	0.01
Co23	8.21	9	0.79

Table S3. Comparison of photocatalytic water oxidation effects of $NiCo_2O_4$-Au-$NiCo_2O_4$ sandwich-type heterojunctions with other catalysts.

Catalyst	O_2 evolution rate/μmol·$h^{-1}g^{-1}$	O_2 evolution rate/μmol·h^{-1}	AQE(%)	Wavelength/nm	Electron acceptor	Reference
$NiCo_2O_4$-Au-$NiCo_2O_4$	6600	33	21.9	450	$Na_2S_2O_8$	*This work*
$NiCo_2O_4$	2810	14.05	10.9	450	$Na_2S_2O_8$	*This work*
Au	318	1.59	0.96	450	$Na_2S_2O_8$	*This work*
$NiCo_2O_4$+Au	2200	11	8.3	450	$Na_2S_2O_8$	*This work*
$CuFeSe_2$@Au	3480	-	7.9	900	$Na_2S_2O_8$	*8*
Au/CuO/Co3O4	2920	-	-	-	$Na_2S_2O_8$	*9*
g-C_3N_4-$CoMn_2O_4$	-	18.3	1.0	380	$AgNO_3$	*10*
1wt Co-g-C_3N_4	-	10.5	-	-	$AgNO_3$	*11*
SA-TCPP	36.1	-	-	-	$AgNO_3$	*12*
$LiTaO_3$	-	2.4	-	-	$AgNO_3$	*13*
$NaTaO_3$	-	4.4	-	-	$AgNO_3$	*14*
WO_3	-	23	-	-	$AgNO_3$	*14*
Fe_2TiO_5-TiO_2	148	-	-	-	$AgNO_3$	*15*
Au/TiO_2-Pt	-	-	1.0	550	$Cr_2O_7^{2-}$	*16*
Ca modified $BaTaO_2N$	-	-	2.1	420	$Cr_2O_7^{2-}$	*17*
CDots-C_3N_4	-	4.1	16	420	-	*18*

References

1 S. B. Wang, B. Y. Guan and X. W. D. Lou, *J. Am. Chem. Soc.,* 2018, **140**, 5037−5040.

2 P. J. Yang, P. J. Ou, Y. X. Fang and X. C. Wang, *Angew. Chem. Int. Ed.,* 2017, **56,** 3992−3996.

3 G. Kresse and J. Hafner, *Phys. Rev. B,* 1994, **49**, 14251−14269.

4 P. E. Blöchl, *Phys. Rev. B,* 1994, **50**, 17953−17979.

5 G.K resse and J. Furthmüller, *Comput. Mater. Sci.*, 1996, **6**, 15−50.

6. M. J. Frisch, G. W. Trucks, H. B. Schlegel, H. Nakatsuji, *Gaussian 09, Revision D. 01, Gaussian, Inc. Wallingford, CT,* 2009, **12**, 3604−3612.

7 A. D. Becke, *J. Chem. Phys.,* 1998, **98**, 5648−5652.

8 H. Wen, H. Li, S. S. He, F. J. Chen, E. L. Ding, S. Liu, B. D. Wang and Y. Peng, *Nanoscale,* 2018, **10**, 2380−2387.

9 G. W. Hu, C.-X. Hu, Z.-Y. Zhu, L. Zhang, Q. Wang and H. L. Zhang, *ACS Sustainable Chem. Eng.,* 2018, **6**, 8801−8808.

10 L. Z. Zhang, C. Yang, Z. Z. Xie and X. C. Wang, *Appl. Catal. B: Environ.,* 2018, **224**, 886−894.

11 G. G. Zhang, C. J. Huang and X. C. Wang, *Small,* 2015, **11**, 9−10.

12 Z. J. Zhang, Y. H. Zhu, X. J. Chen, H. J. Zhang and J. Wang, *Adv. Mater.,* 2019, **31**, 1806626.

13 H. Kato, A. Kudo, Water splitting into H_2 and O_2 on alkali tantalate photocatalysts $ATaO_3$ (A=Li, Na, and K). *J. Phys. Chem. B,* 2001, **105**, 4285−4292.

14 J. Ke, H. R. Zhou, J. Liu, X. G. Duan, H. Y. Zhang, S. M. Liu and S. B. Wang, *J. Colloid Interf. Sci.,* 2018, **514,** 576−583.

15 M. Waqas, S. Iqbal, A. Bahadur, A. Saeed, M. Raheel, M. Javed, *Appl. Catal. B: Environ.,* 2017, **219**, 30−35.

16 A. Tanaka, K. Nakanishi, R. Hamada, K. Hashimoto and H. Kominami, *ACS Catal.,* 2013, **3**, 1886−1891.

17 S. H. Wei, G. Zhang and X. X. Xu, *Appl. Catal. B: Environ.,* 2018, **237**, 373−381.

18 J. Liu, Y. Liu, N. Y. Liu, Y. Z. Han, X. Zhang, H. Huang, Y. Lifshitz, S.-T. Lee, J. Zhong and Z. H. Kang, *Science,* 2015, **347**, 970−974.